



# Multidimensional Small Baseline Subset (MSBAS) for Two-Dimensional Deformation Analysis: Case Study Mexico City

Sergey V. Samsonov & Nicolas d'Oreye

To cite this article: Sergey V. Samsonov & Nicolas d'Oreye (2017) Multidimensional Small Baseline Subset (MSBAS) for Two-Dimensional Deformation Analysis: Case Study Mexico City, Canadian Journal of Remote Sensing, 43:4, 318-329, DOI: [10.1080/07038992.2017.1344926](https://doi.org/10.1080/07038992.2017.1344926)

To link to this article: <https://doi.org/10.1080/07038992.2017.1344926>



Accepted author version posted online: 05 Jul 2017.  
Published online: 21 Jul 2017.



Submit your article to this journal [↗](#)



Article views: 214



View Crossmark data [↗](#)



Citing articles: 5 View citing articles [↗](#)



## Multidimensional Small Baseline Subset (MSBAS) for Two-Dimensional Deformation Analysis: Case Study Mexico City

Sergey V. Samsonov <sup>a</sup> and Nicolas d'Oreye <sup>b,c</sup>

<sup>a</sup>Natural Resources Canada, 560 Rochester Street, Ottawa, ON K1A 0E4, Canada; <sup>b</sup>European Center for Geodynamics and Seismology, Rue Josy Welter 19, L-7256 Walferdange, Grand-Duchy of Luxembourg; <sup>c</sup>National Museum of Natural History, Department of Geophysics/Astrophysics, Rue Josy Welter 19, L-7256 Walferdange, Grand-Duchy of Luxembourg

### ABSTRACT

Time series of ground deformation are used to describe motion produced by various natural and anthropogenic processes, such as earthquakes, volcanic eruptions, landslides, subsidence due to resource exploitation, and uplift due to fluid injection. Presented here, the multidimensional small baseline subset (MSBAS) technique simultaneously processes multiple ascending and descending DInSAR datasets and produces 2-D, horizontal east-west and vertical, deformation time series with combined temporal resolution over overlapped area. The set of linear equations that comprises MSBAS is usually rank deficient and is solved in the least-square sense by applying the singular value decomposition (SVD) and the zero-, first-, or second-order Tikhonov regularization. The MSBAS source code is written in C++ and is linked to the linear algebra package (LAPACK) library that provides SVD support. For demonstration of capabilities, MSBAS is used to compute 2-D deformation time series of Mexico City by simultaneously processing ascending and descending RADARSAT-2 data acquired during October 2008–December 2012. This area is known to subside due to excessive groundwater extraction that produces pore water pressure drop and compaction of highly compressible clays. During the studied period we observed subsidence with rates over 35 cm/year and horizontal motion of up to 5 cm/year. The MSBAS software can be downloaded from <http://insar.ca/>.

### RÉSUMÉ

Les séries temporelles de déformation du sol sont utilisées pour décrire le mouvement produit par divers processus naturels et anthropiques, tels que les séismes, les éruptions volcaniques, les glissements de terrain, l'affaissement dû à l'exploitation des ressources et le soulèvement dû à l'injection de fluides. Dans la présente étude, la méthode d'analyse multidimensionnelle à l'aide de sous-ensembles à courte ligne de base (MSBAS) traite simultanément plusieurs ensembles de données DInSAR ascendantes et descendantes et produit des séries temporelles bidimensionnelles, horizontales (est-ouest) et verticales, avec une résolution temporelle combinée sur la zone commune à toutes les données. L'ensemble des équations linéaires qui comprend MSBAS est habituellement déficient de rang et est résolu en utilisant une méthode par moindres carrés en appliquant la décomposition en valeurs singulières (SVD) et la régularisation Tikhonov d'ordre zéro, du premier ou du deuxième ordre. Le code source MSBAS est écrit en C++ et est lié à la bibliothèque package (LAPACK) d'algèbre linéaire qui fournit un support SVD. Pour une démonstration de ses capacités, MSBAS est utilisé pour calculer des séries temporelles de déformation bidimensionnelle de Mexico en traitant simultanément les données ascendantes et descendantes de RADARSAT-2 acquises d'octobre 2008 à décembre 2012. Cette zone est connue pour l'affaissement dû à l'extraction excessive d'eau souterraine qui produit une chute de pression d'eau interstitielle et un compactage des argiles hautement compressibles. Au cours de la période d'étude, nous avons observé un affaissement avec des taux supérieurs à 35 cm/an et un mouvement horizontal jusqu'à 5 cm/an. Le logiciel MSBAS peut être téléchargé à partir de <http://insar.ca/>.

### ARTICLE HISTORY

Received 31 October 2016  
Accepted 10 May 2017

## Introduction

Differential interferometric synthetic aperture radar (DInSAR) measures ground deformation from repeatedly acquired air and spaceborne synthetic aperture radar (SAR) data (Massonnet and Feigl 1998; Rosen et al. 2000). The 1-D line-of-sight DInSAR measurements are complementary to the 3-D Global Navigation Satellite System

(GNSS; Hofmann-Wellenhof et al. 2001) measurements (Gudmundsson et al. 2002; Samsonov et al. 2007, 2008). The GNSS time series of daily solutions provide complete information about receiver position as a function of time (e.g., Zhang et al. 1997). The spatial resolution of 3-D GNSS observations is limited to locations of receivers and is usually larger than a few kilometers. On the contrary,

1-D line-of-sight DInSAR measurements have very dense spatial resolution of a few meters or better but sparse temporal resolution, defined by satellite revisit time (e.g., 6 days for Sentinel-1A/B, 14 days for ALOS-2, and 24 days for RADARSAT-2). Airborne SAR data can potentially be acquired more frequently but due to high acquisition cost this rarely happens. Both DInSAR and GNSS are used in a variety of geophysical applications: for studying earthquakes (Bock et al. 1997; Beavan et al. 2010, 2011); volcanic eruptions (Biggs et al. 2010; Samsonov et al. 2011a, 2016a); landslides (Ding et al. 2000); subsidence and uplift due to resource exploitation, urbanization, carbon sequestration, and fluid injection (Schmidt and Burgmann 2003; Gourmelen et al. 2007; Strozzi et al. 2011; Teatini et al. 2011; Dong et al. 2013).

Differential interferograms are computed from pairs of master and slave SAR images acquired by the same or similar sensor at 2 different times. After initial processing, consisting of slave image co-registration and re-sampling into master geometry, interferogram formation, removal of earth curvature and topographic phases, filtering and phase unwrapping, differential interferograms capture the line-of-sight motion occurring between 2 acquisitions. Interferograms are often contaminated by noise of various magnitude and distribution, for example, due to phase decorrelation, atmospheric disturbances, and residual topography (Li et al. 2005; Samsonov 2010; Fournier et al. 2011; Samsonov et al. 2014d).

Time series of 1-D line-of-sight deformation are computed from a set of highly coherent interferograms acquired with small temporal and spatial baselines using the small baseline subset (SBAS) technique (Berardino et al. 2002; Lanari et al. 2004; Samsonov et al. 2011b). The temporal resolution of produced time series is defined by satellite revisit time and their spatial resolution and coverage are similar to those of interferograms.

Presented here, the multidimensional small baseline subset (MSBAS) technique computes 2-D, horizontal east-west and vertical, time series of ground deformation from ascending and descending DInSAR data acquired by various SAR sensors with different acquisition parameters, such as azimuth and incidence angles, spatial resolution, and wavelength. Produced 2-D time series have combined temporal resolution and near daily temporal resolution can be achieved by simultaneous processing data from multiple SAR sensors. The MSBAS technique is more suitable for retrieving 2-D horizontal and vertical deformation analysis associated with land subsidence; it is less suitable for earthquake-, landslide-, and glacier-related deformation studies where there is a possibility of a large N-S displacement component. MSBAS has already been used for measuring ground deformation due to mining (Samsonov et al. 2013a, 2013b, 2014b), urban

development (Samsonov et al. 2014a), carbon sequestration (Samsonov et al. 2015; Czarnogorska et al. 2016), permafrost aggradation and pingo growth (Samsonov et al. 2016b), and volcanic activities (Samsonov and d'Oreye 2012; Smets et al. 2014; Samsonov et al. 2014c, 2014d, 2016a). Implementation of the MSBAS software, control parameters, processing options, and an implicit set of equation for a simplified case are described.

For demonstration of capabilities, MSBAS is used to compute 2-D deformation time series over Mexico City during October 2008–December 2012, by simultaneously processing ascending and descending fine resolution RADARSAT-2 data. Mexico City experiences one of the fastest subsidence in the world caused by excessive ground water withdrawal that produces pore water pressure drop and compaction of highly compressible clays (Ortega-Guerrero et al. 1993, 1999; Ortiz-Zamora and Ortega-Guerrero 2010; Ruiz and Ruiz 2013; Gambolati and Teatini 2015). A regional stratigraphic cross section of the area can be found in Ortega-Guerrero et al. (1999). Cumulative subsidence in Mexico City reached 13 m in 2006, and under current pumping rates will reach 19 meters by 2020 (Ortiz-Zamora and Ortega-Guerrero 2010). Subsidence in Mexico City was previously investigated with various DInSAR techniques (e.g., Chaussard et al. 2014; Osmanoglu et al. 2016). Previous deformation maps were of coarse spatial resolution and of limited coverage, and time series analysis was limited to 1-D line-of-sight ascending/descending measurements.

### Multidimensional small baseline subset technique

The MSBAS technique computes 2-D, horizontal east-west and vertical, deformation time series from overlapped in time and space ascending and descending DInSAR data:

$$\begin{pmatrix} \hat{A} \\ \lambda L \end{pmatrix} \begin{pmatrix} V_E \\ V_U \end{pmatrix} = \begin{pmatrix} \hat{\Phi} \\ 0 \end{pmatrix}, \quad (1)$$

where matrix  $\hat{A} = \{s_E A, s_U A\}$  consists of time intervals between consecutive SAR acquisitions  $A$  (for an example of  $A$ , see Samsonov [2010]) and east and up components of a line-of-sight vector  $s = \{s_E, s_U\} = \{-\cos \theta \sin \phi, \cos \phi\}$ ,  $\theta$  is azimuth and  $\phi$  is incidence angles,  $V_E$  and  $V_U$  represent unknown horizontal east-west and vertical velocities that are to be determined,  $\hat{\Phi}$  represents observed DInSAR data, geocoded and resampled to a common grid,  $\lambda$  is a regularization parameter, and  $L$  is a zero-, first-, or second-order difference operator. The unknown parameters  $V_E$  and  $V_U$  for each pixel are solved by applying the singular value decomposition (SVD) and deformation time series are reconstructed from the computed deformation rates by numerical integration.



$$\begin{pmatrix}
s_E^{asc} \Delta t_1 & s_U^{asc} \Delta t_1 & s_E^{asc} \Delta t_2 & s_U^{asc} \Delta t_2 & 0 & 0 & 0 & 0 & 0 & 0 \\
0 & 0 & 0 & 0 & s_E^{asc} \Delta t_3 & s_U^{asc} \Delta t_3 & s_E^{asc} \Delta t_4 & s_U^{asc} \Delta t_4 & 0 & 0 \\
0 & 0 & 0 & 0 & 0 & 0 & 0 & 0 & s_E^{asc} \Delta t_5 & s_U^{asc} \Delta t_5 \\
s_E^{dsc} \Delta t_1 & s_U^{dsc} \Delta t_1 & 0 & 0 & 0 & 0 & 0 & 0 & 0 & 0 \\
0 & 0 & s_E^{dsc} \Delta t_2 & s_U^{dsc} \Delta t_2 & s_E^{dsc} \Delta t_3 & s_U^{dsc} \Delta t_3 & 0 & 0 & 0 & 0 \\
0 & 0 & 0 & 0 & 0 & 0 & s_E^{dsc} \Delta t_4 & s_U^{dsc} \Delta t_4 & s_E^{dsc} \Delta t_5 & s_U^{dsc} \Delta t_5 \\
\lambda & 0 & -\lambda & 0 & 0 & 0 & 0 & 0 & 0 & 0 \\
0 & \lambda & 0 & -\lambda & 0 & 0 & 0 & 0 & 0 & 0 \\
0 & 0 & \lambda & 0 & -\lambda & 0 & 0 & 0 & 0 & 0 \\
0 & 0 & 0 & \lambda & 0 & -\lambda & 0 & 0 & 0 & 0 \\
0 & 0 & 0 & 0 & \lambda & 0 & -\lambda & 0 & 0 & 0 \\
0 & 0 & 0 & 0 & 0 & \lambda & 0 & -\lambda & 0 & 0 \\
0 & 0 & 0 & 0 & 0 & 0 & \lambda & 0 & -\lambda & 0 \\
0 & 0 & 0 & 0 & 0 & 0 & 0 & \lambda & 0 & -\lambda
\end{pmatrix}
\begin{pmatrix}
V_1^E \\
V_1^U \\
V_2^E \\
V_2^U \\
V_3^E \\
V_3^U \\
V_4^E \\
V_4^U \\
V_5^E \\
V_5^U
\end{pmatrix}
=
\begin{pmatrix}
\Phi_1^{asc} \\
\Phi_2^{asc} \\
\Phi_3^{asc} \\
\Phi_1^{dsc} \\
\Phi_2^{dsc} \\
\Phi_3^{dsc} \\
0 \\
0 \\
0 \\
0 \\
0 \\
0 \\
0 \\
0
\end{pmatrix}, \quad (4)$$

$$\begin{pmatrix}
s_E^{asc} \Delta t_1 & s_U^{asc} \Delta t_1 & s_E^{asc} \Delta t_2 & s_U^{asc} \Delta t_2 & 0 & 0 & 0 & 0 & 0 & 0 \\
0 & 0 & 0 & 0 & s_E^{asc} \Delta t_3 & s_U^{asc} \Delta t_3 & s_E^{asc} \Delta t_4 & s_U^{asc} \Delta t_4 & 0 & 0 \\
0 & 0 & 0 & 0 & 0 & 0 & 0 & 0 & s_E^{asc} \Delta t_5 & s_U^{asc} \Delta t_5 \\
s_E^{dsc} \Delta t_1 & s_U^{dsc} \Delta t_1 & 0 & 0 & 0 & 0 & 0 & 0 & 0 & 0 \\
0 & 0 & s_E^{dsc} \Delta t_2 & s_U^{dsc} \Delta t_2 & s_E^{dsc} \Delta t_3 & s_U^{dsc} \Delta t_3 & 0 & 0 & 0 & 0 \\
0 & 0 & 0 & 0 & 0 & 0 & s_E^{dsc} \Delta t_4 & s_U^{dsc} \Delta t_4 & s_E^{dsc} \Delta t_5 & s_U^{dsc} \Delta t_5 \\
\lambda & 0 & -2\lambda & 0 & \lambda & 0 & 0 & 0 & 0 & 0 \\
0 & \lambda & 0 & -2\lambda & 0 & \lambda & 0 & 0 & 0 & 0 \\
0 & 0 & \lambda & 0 & -2\lambda & 0 & \lambda & 0 & 0 & 0 \\
0 & 0 & 0 & \lambda & 0 & -2\lambda & 0 & \lambda & 0 & 0 \\
0 & 0 & 0 & 0 & \lambda & 0 & -2\lambda & 0 & \lambda & 0 \\
0 & 0 & 0 & 0 & 0 & \lambda & -2\lambda & 0 & \lambda & 0 \\
0 & 0 & 0 & 0 & 0 & 0 & 0 & -2\lambda & 0 & \lambda
\end{pmatrix}
\begin{pmatrix}
V_1^E \\
V_1^U \\
V_2^E \\
V_2^U \\
V_3^E \\
V_3^U \\
V_4^E \\
V_4^U \\
V_5^E \\
V_5^U
\end{pmatrix}
=
\begin{pmatrix}
\Phi_1^{asc} \\
\Phi_2^{asc} \\
\Phi_3^{asc} \\
\Phi_1^{dsc} \\
\Phi_2^{dsc} \\
\Phi_3^{dsc} \\
0 \\
0 \\
0 \\
0 \\
0 \\
0 \\
0 \\
0
\end{pmatrix}. \quad (5)$$

In Equations (3)–(5), regularization parameter  $\lambda$  is introduced in order to regularize the solution. Large  $\lambda$  produces a smooth solution and the optimal value can be selected, for example, with the L-curve method (Hansen and O’Leary 1993).

The choice of regularization order depends on the signal characteristics and study objectives. In case of the zero-order regularization, the solution is found by the least squares fitting of data and by minimizing the solution norm (i.e., deformation rates between consecutive acquisitions  $V_E$  and  $V_U$ ). This type of regularization should be used when the mean of the deformation rates is expected to be close to zero (e.g., oscillating motion). If such methodology is used for describing a steady motion then the solved deformation rates will likely be smaller than the actual due to the bias introduced by minimization of solution norm.

The 2-D time series of cumulative deformation are then reconstructed in the following way:

$$d_i^E = \sum_{i=1}^5 V_i^E \Delta t_i, \quad d_i^U = \sum_{i=1}^5 V_i^U \Delta t_i. \quad (6)$$

### MSBAS control parameters

Control parameters are designed to control processing flow of the MSBAS software (Figure 2, Table 1) and are listed in a header file (Listing 1). The *FORMAT* parameter controls format of the input data, 4 bytes float small endian and 4 bytes float big endian formats are supported. The *FILE\_SIZE* parameter controls the number of columns and rows in resampled to a common grid interferograms. The *WINDOW\_SIZE* parameter controls location and size of the sub-region to be processed. This

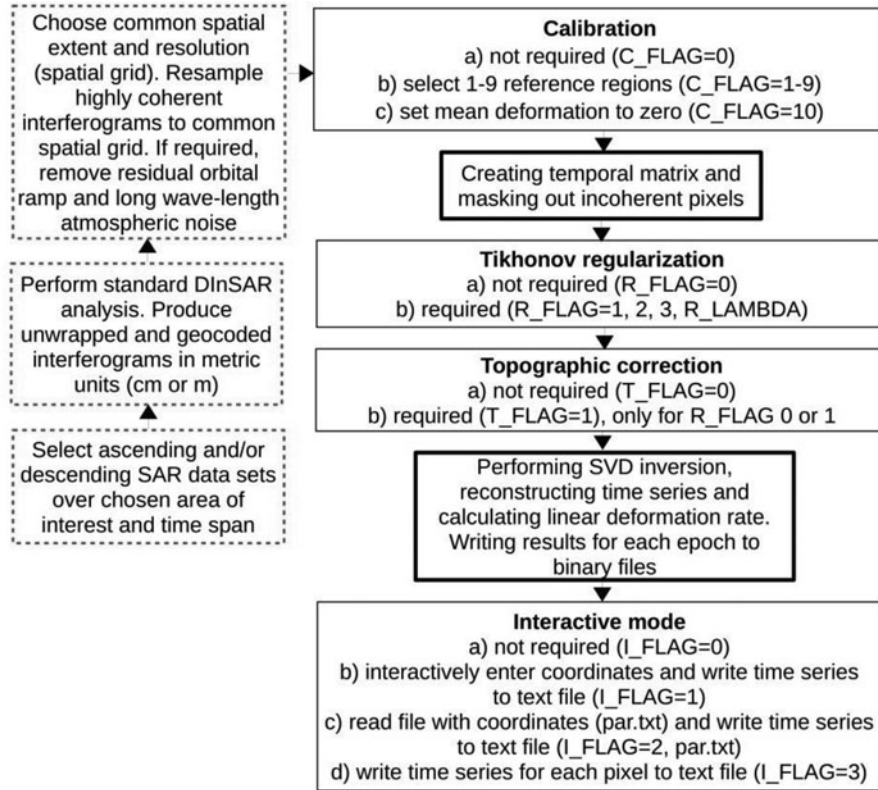


**Figure 2.** Flowchart diagram of MSBAS processing algorithm. The first three processing steps in dashed boxes are performed outside of this software. Processing steps outlined in thick black are mandatory and cannot be manipulated. Processing steps outlined in thin black are optional and can be manipulated by specifying appropriate processing flags.

**Table 1.** MSBAS parameters and supported processing options must have only one uniquely named parameter in header file. Detailed description is provided in text.

Parameter	Type	Value(s)	Description
FORMAT	int	0	4 bytes float, small endian
FORMAT	int	1	4 bytes float, big endian
FILE_SIZE	int(s)	$x, y$	For example, 1000, 1000
WINDOW_SIZE	int(s)	$x_a, x_b, y_a, y_b$	Default: 0, $x-1$ , 0, $y-1$
C_FLAG	int	0	No calibration
C_FLAG	int(s)	1, $x_1, y_1, \Delta x, \Delta y$	1 reference region
C_FLAG	int(s)	2, $x_1, y_1, x_2, y_2, \Delta x, \Delta y$	2 reference regions
C_FLAG	int	10	Average set to zero
R_FLAG	int	0	No regularization
R_FLAG	int, float	1, $\lambda$	Zero order regularization
R_FLAG	int, float	2, $\lambda$	First order regularization
R_FLAG	int, float	3, $\lambda$	Second order regularization
T_FLAG	int	0	No topographic correction
T_FLAG	int	1	Topographic correction
I_FLAG	int	0	No interactive mode
I_FLAG	int	1	Interactive mode
I_FLAG	int, s	2, <i>par.txt</i>	Process <i>par.txt</i> file
I_FLAG	int	3	Save everything in text file
SET	s, int, int, s	<i>hhmmss, <math>\theta, \varphi, set.txt</math></i>	For example, 122435, -189, 34, <i>dsc.txt</i>
#			Comment

Note. Type *s* means *string*.  $x$  and  $y$  are width and length of interferograms.  $x_a, x_b, y_a, y_b$  are first and last columns and rows of sub-region to be processed.  $x_i$  and  $y_i$  are column number and row number of reference region(s), up to 9 regions are supported.  $\Delta x$  and  $\Delta y$  are half-width/length of reference region(s).  $\lambda$  is regularization parameter. *hhmmss* is acquisition time for each set (must be 6 symbols).  $\theta$  and  $\varphi$  are azimuth and incidence angles, measured in degrees. Lines can be commented with # symbol.



**Listing 1.** Example of MSBAS *header.txt* file used for processing RADARSAT-2 data over Mexico City.

```

FORMAT = 1
FILE_SIZE = 2256, 2311
WINDOW_SIZE = 0, 2255, 0, 2310
R_FLAG = 2, 0.03
C_FLAG = 2, 1804, 1560, 822, 370, 64, 64
T_FLAG = 0
I_FLAG = 2, par.txt
SET = 004903, 349.0744254, 42.5462, asc.txt
SET = 121952, -169.6351440, 48.5069, dsc.txt

```

parameter helps to reduce memory requirements and execution time when processing of the entire region is not required. The calibration *C\_FLAG* parameter controls the way each interferogram is calibrated. The most common approach is to select a single reference region, but up to 9 reference regions of the same size are supported. It is also possible to disable calibration or to set the average value of each interferogram to zero. The regularization *R\_FLAG* parameter controls the order of regularization (none, zero, first, second) and the value of regularization parameter  $\lambda$ . The topographic correction *T\_FLAG* parameter allows to solve for deformation rates and the residual topography, as it was done in Samsonov et al. (2011b). It can be used only for non-regularized (2) or zero-order regularized (3) problems. The interactive *I\_FLAG* parameter invokes an interactive mode that allows to write time series for specified pixels (Listing 2) to the individual text files. The *SET* parameter defines DInSAR datasets; it accepts the acquisition time (*hhmmss*),  $\theta$  and  $\varphi$ , the azimuth and incidence angles measured in degrees, and a file with a list of interferograms. The file with a list of interferograms contains in each line a path to the interferogram file, perpendicular baseline in meters, and slave and master acquisition dates in YYYYMMDD format (Listings 3 and 4). If only ascending or descending datasets are provided, then SBAS algorithm is applied

**Listing 2.** Example of MSBAS *par.txt* file.

```

992 1103 2
1003 1273 2
1227 1948 2
1256 1498 2
...

```

**Listing 3.** Example of MSBAS *asc.txt* file.

```

...
../dsc/dint/20100226_HH_20100415_HH.msbase 256.43700 20100226 20100415
../asc/dint/20100226_HH_20100509_HH.msbase 313.60080 20100226 20100509
..., 117 lines

```

**Listing 4.** Example of MSBAS *dsc.txt* file.

```

...
../dsc/dint/20100221_HH_20100410_HH.msbase -271.21860 20100221 20100410
../dsc/dint/20100221_HH_20100504_HH.msbase -108.57100 20100221 20100504
..., 147 lines

```

instead and the line-of-sights results are computed as described in Samsonov et al. (2011b).

## MSBAS output products

The output of MSBAS software consists of files with the 2-D cumulative deformation for each acquisition epoch. File dimensions and units are those as in input interferograms. The 2-D annual linear deformation rates and their standard deviations are computed by fitting a line to time series. In case of nonlinear deformation, the linear deformation rates can be misleading and need to be treated with caution. If topographic correction is selected then a file with perpendicular baseline versus observed phase regression values is created. The time matrix is stored in a text file; it can be used, for example, by *R* software for rank and singular values analysis. If interactive mode is selected with *I\_FLAG* = 3 then a text file with time series for all pixels is created. For diagnostic purposes solution and residual norms are also stored in separate files. All screen output is stored in a log file.

## MSBAS software implementation

The MSBAS software is written in C++ programming language using a standard template library and exception handling. It is linked to the Linear Algebra PACKage (LAPACK, <http://www.netlib.org/lapack/>) library that provides SVD support. The NetBeans (<http://netbeans.org>) software development environment is used for debugging on Linux 64-bit platform. The MSBAS source code does not require NetBeans and potentially can be recompiled under any standard operational system, such as Windows or Mac.

## Mexico City case study

For studying ground subsidence in Mexico City (Figure 3) we collected 36 ascending Multi-Look Fine 3 (MF3) images spanning 20080425–20101211 and 43 descending Multi-Look Fine 6 (MF6) images spanning 20081029–20111201 from RADARSAT-2 satellite (Figure 4). All ascending and descending images were used in SBAS processing but only 30 ascending and 30 descending images with overlapped temporal coverage were used in MSBAS processing (Table 2).

Each SAR dataset was processed independently with the GAMMA software (Wegmuller and Werner 1997) in the following way. A single master for each set was selected and remaining images were re-sampled into the master geometry. The 7 in range and 7 in azimuth multi-looked (i.e., spatially averaged) interferograms were computed and the topographic phase was removed using the

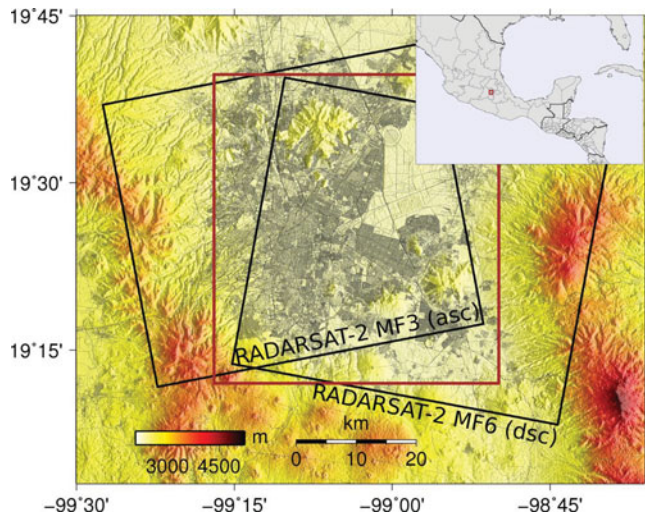


**Figure 3.** Shuttle Radar Topography Mission Digital Elevation Model of Mexico City. Ascending and descending RADARSAT-2 frames are outlined in black. Location of study site is outlined in brown. Black lines are transportation routes (<http://mapzen.com/>).

30-m resolution Shuttle Radar Topography Mission Digital Elevation Model. Differential interferograms were filtered using the adaptive filtering with a filtering function based on local fringe spectrum (Goldstein and Werner 1998) and unwrapped using the minimum cost flow algorithm (Costantini 1998). The residual orbital ramp was corrected by applying baseline refinement. The area experiencing large ground deformation was masked out and a procedure implemented in GAMMA software that re-estimates baseline parameters based on the measurement of interferometric phase and topographic height was applied. Minor interpolation of each interferogram was performed in order to improve the spatial coverage reduced by decorrelation. This process is described in greater detail in Samsonov et al. (2011a). Then,

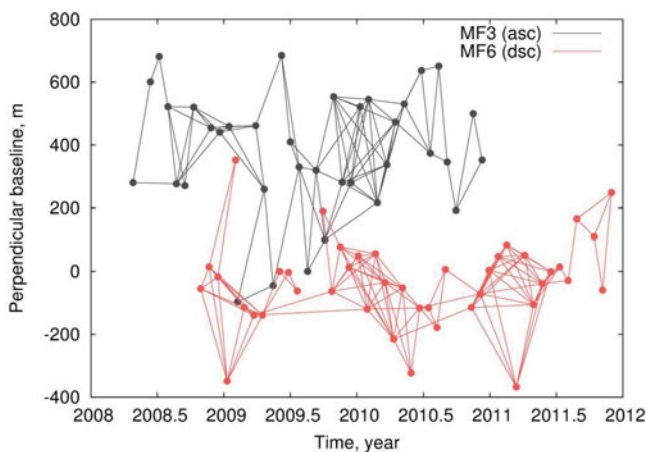


**Figure 4.** Perpendicular baseline and time span of automatically selected RADARSAT-2 ascending Multi-Look Fine 3 (MF3) and descending Multi-Look Fine 6 (MF6) interferograms used in this study.

**Table 2.** SAR datasets used in MSBAS processing: RADARSAT-2 Multi-Look Fine 3 and 6 (MF3, MF6); time span (in YYYYMMDD format), range-azimuth resolution, azimuth  $\theta$  and incidence  $\varphi$  angles, number of available SAR images  $N$ , and number of calculated interferograms  $M$  for each data set.

InSAR Set	Time Span	Resolution, m	$\theta^\circ$	$\varphi^\circ$	$N$	$M$
R2-MF3 (asc)	20080730–20101211	3.1–4.6	349	43	30	117
R2-MF6 (dsc)	20081029–20110616	3.1–4.6	–170	49	30	147
Total	20081029–20101211				58	264

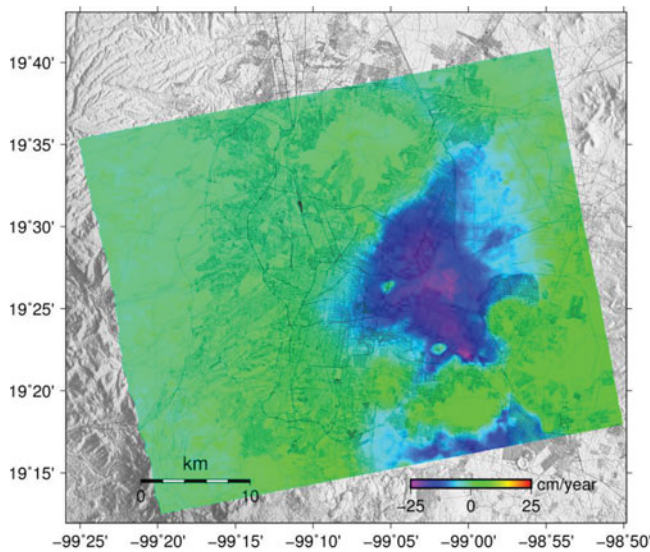
ascending and descending interferograms were geocoded and resampled using GMT (<http://gmt.soest.hawaii.edu/>) scripts to a common lat/long grid with the uniform spatial sampling of 20 m.

The SBAS technique was applied to each ascending and descending dataset individually to produce the line-of-sight time series and the annual linear deformation rate. The SBAS line-of-sight deformation rates are shown in Figure 5. Broad subsidence is observed around Mexico City with the maximum line-of-sight deformation rate of about 25 cm/year. The spatial coverage of a descending set is affected by decorrelation, exposing Digital Elevation Model (DEM) background in Figure 5b.

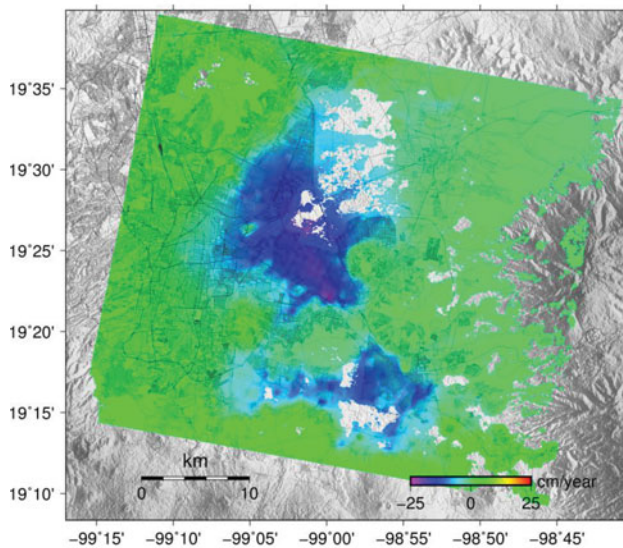
The MSBAS technique was applied to ascending and descending datasets simultaneously to produce horizontal east-west and vertical time series and annual linear deformation rates. The first order regularization with  $\lambda$  equal to 0.03 was chosen according to the L-curve analysis in Figure 6. Two reference regions were selected: NW and SE of subsiding areas. The computed horizontal east-west and vertical deformation rate maps are shown in Figure 7 and 8 latitudinal profiles are shown in Figure 8. The horizontal map shows a moderate NW-SE trend, which is likely processing artifact, however, tectonic motion cannot be ruled out. Horizontal east-west profile at latitude 19.32° shows 2 regions with abrupt changes in deformation rates. Subsidence can also cause horizontal motion towards the center of a subsidence bowl (Samiee-Esfahany et al. 2009; Samsonov et al. 2013b, 2016c). If required the trend in a horizontal map can be removed by fitting and subtracting a plane with, for example, GMT *grdtrend* command. Maximum magnitude of horizontal motion is less than 5 cm/year. Ground subsidence with a rate of up to 35 cm/year is observed. Spatial variability of subsidence can be observed, for example, in profiles at latitudes of 19.40° and 19.44°. The first profile shows very abrupt subsidence at longitude –98.98°, and the second profile shows a non-subsiding region at longitude –99.09°. Vertical profiles at latitudes 19.56° and 19.52° are asymmetric, with a larger gradient on the western side.

For points P1–P9, the time series are shown in Figure 9. Steady subsidence is observed at all points and is largest at P7. Eastward motion is observed at P1, P2, and P6 and





(a) RADARSAT-2 MF3 (asc)



(b) RADARSAT-2 MF6 (desc)

**Figure 5.** Line-of-sight ascending (a) and descending (b) linear-deformation rates calculated with small baseline subset (SBAS) technique. Background is Shuttle Radar Topography Mission Digital Elevation Model.

westward motion is observed at P8 and P9. The volume of subsidence is equal to  $93.6 \times 10^6 \text{ m}^3/\text{year}$ .

## Discussion and conclusions

Presented MSBAS technique computes horizontal east-west and vertical deformation time series from multiple ascending and descending DInSAR data. The MSBAS technique is an extension of the SBAS technique (Berardino et al. 2002; Lanari et al. 2004; Samsonov et al. 2011b) that computes 1-D line-of-sight time series. The north-south component of deformation cannot be computed from the ascending and descending data alone

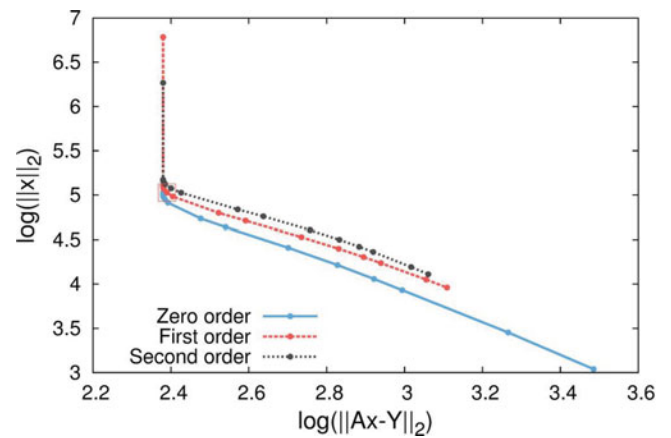


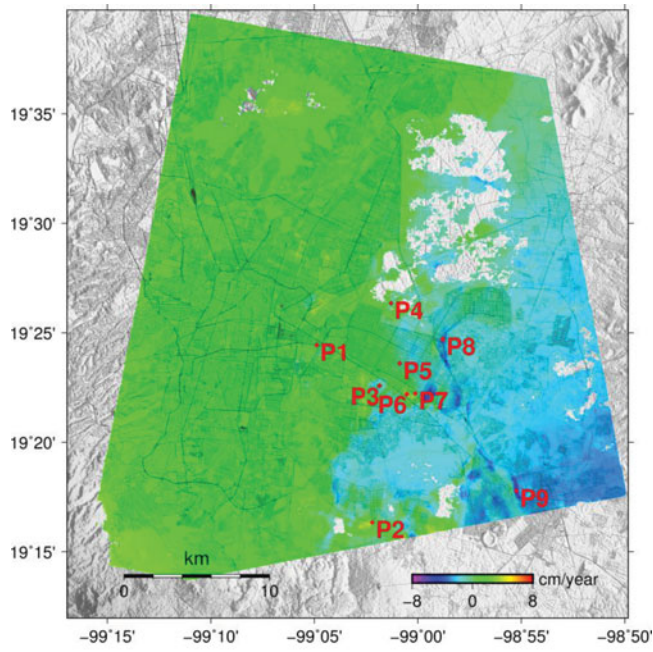
**Figure 6.** L-curve for zero, first, and second order regularizations for  $\lambda$  values in range 0.00001–1.0. Optimal value of 0.03 (marked) for first order regularization is used in this study.

because of low sensitivity of near-polar orbiting sensors on sun-synchronous orbits to north-south deformation. The 3-D solution can potentially be computed with MSBAS if data from 3 different orbital geometries is used. This, for example, can be achieved with airborne data or by combining spaceborne and airborne data. The 3-D analysis is not implemented in the current version of MSBAS software.

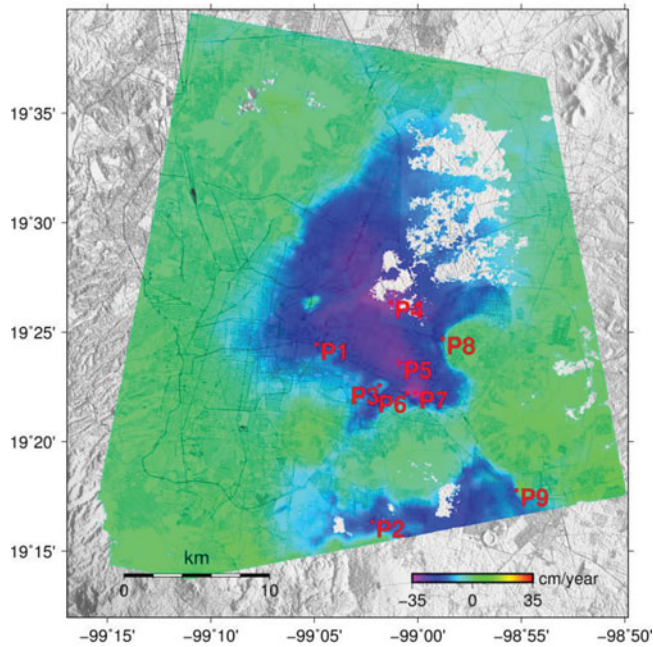
The MSBAS software is written in C++ and is linked to the LAPACK library that provides SVD support. The MSBAS processing time depends on the number of interferograms and grid dimensions and is usually less than 30 minutes on a standard PC. The current version of MSBAS is a single threaded application but multiprocessing support can be implemented in order to reduce processing time.

The solution produced by MSBAS is approximate in a sense that it neglects contribution of north-south component. While this contribution is not large, about 6%–15% (i.e., equal to the unaccounted north component of the line-of-sight vector  $s_N = \sin \theta \sin \varphi$ ), it can become significant in case of a disproportionately large (in comparison to eastward and vertical motion) north-south motion that can be produced by earthquakes or landslides. The exact magnitude of impact of north-south motion on MSBAS horizontal east-west and vertical time series depends on the number of DInSAR datasets and their acquisition geometry, particularly incidence angles, since azimuth angles of spaceborne acquisitions are fixed. A simple numeric simulation using the actual time matrix can be employed to measure this impact.

Analyzing various time matrices we observed that: (i) horizontal east-west and vertical components of deformation do not impact each other if temporal resolution of ascending and descending acquisitions is sufficiently high; (ii) the impact of north-south motion



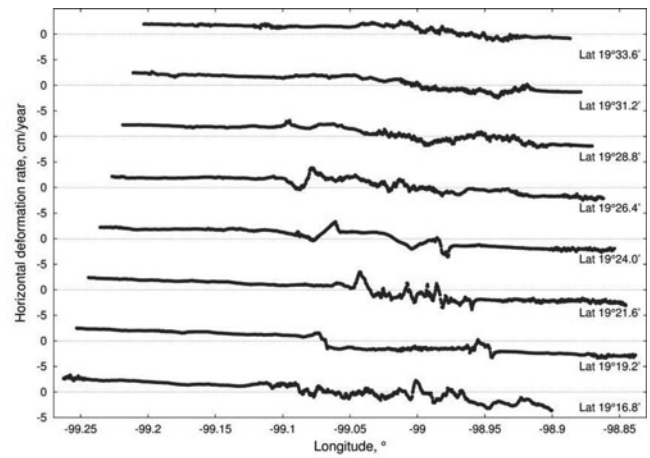
(a) Horizontal east-west



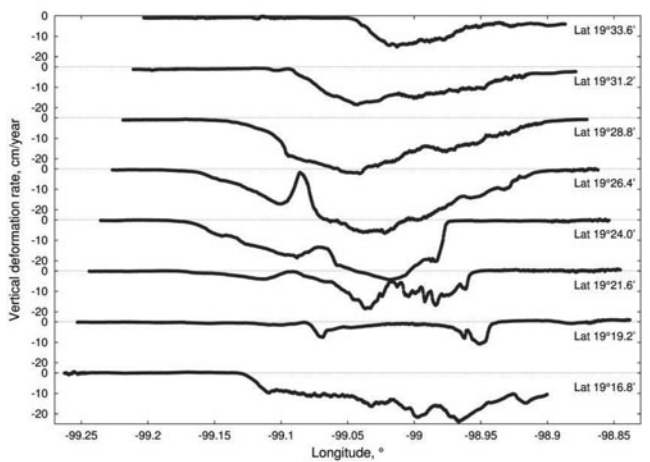
(b) Vertical

**Figure 7.** Horizontal east-west and vertical linear deformation rates calculated with multidimensional small baseline subset (MSBAS) technique. For points P1–P9 time series of ground deformation are provided in Figure 9. Background is Shuttle Radar Topography Mission Digital Elevation Model.

on vertical component is of opposite sign, for example, positive northern motion will produce negative signal of a smaller magnitude in the vertical component; (iii) impact of north-south motion on horizontal east-west



(a)



(b)

**Figure 8.** Latitudinal profiles across horizontal east-west (a) and vertical (b) linear deformation rates calculated with multidimensional small baseline subset (MSBAS) technique.

component becomes negligible when incidence angles of all datasets are equal.

Time series produced from sparse ascending and descending DInSAR data acquired at different times may display artifacts. For example, if an interferogram computed from an ascending slave image acquired at time  $t_i$  does not observe a rapid signal occurring between  $t_i$  and  $t_{i+1}$  but an interferogram computed from a descending slave image acquired at time  $t_{i+1}$  observes this signal, then this signal will be interpreted incorrectly until the next ascending interferogram is computed with slave image acquired at time  $t_{i+2}$ . Appearance of such artifacts is minimized by applying regularization but never fully corrected. This effect must be considered when interpreting rapid, in comparison with temporal resolution, deformation. In order to improve the quality of time series, the temporal resolution of data must be increased, which can be achieved, for example, by using data from more than 2 datasets.



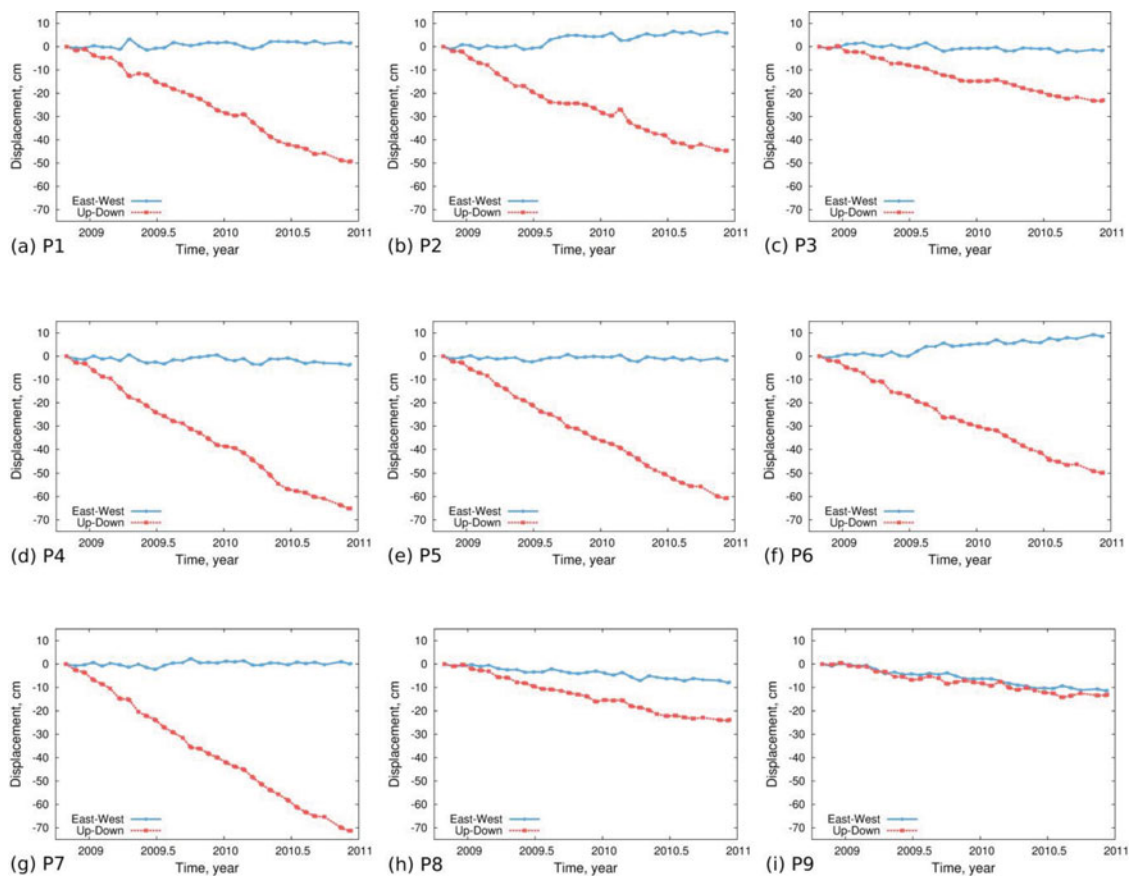


**Figure 9.** Horizontal east-west and vertical time series of ground deformation for points P1–P9 from Figure 7 computed with MSBAS. Subsidence is observed at all points and is largest at P7. Eastward motion is observed at P1, P2, P6 and westward motion is observed at P3, P8, P9.

Further development of the MSBAS software is feasible and desirable. The current version produces time series only for pixels coherent in all interferograms. The spatial coverage can be presently improved by interpolating within small radius gaps in individual interferograms, or by selecting a smaller, more coherent subset of interferograms. It is desirable to be able to compute time series for pixels; coherent only in some interferograms (for example, prior to significant land cover change).

Precision of MSBAS time series can be estimated using simulated data applied to the actual time matrix. It is desirable, however, to develop the mathematical framework for computing precision based on a form of time matrix and precision of interferograms.

Application of the MSBAS technique to measuring ground deformation in Mexico City confirmed previous results computed from 2007–2011 ALOS data (Chausard et al. 2014). The subsidence rate observed in this and previous studies are very similar but horizontal motion is resolved better in this study due to higher resolution data used and larger number of images. The cause of subsidence is excessive ground water withdrawal that produces pore water pressure drop and compaction of highly compressible clays. Similar to the previous study

of Osmanoglu et al. (2016), we did not observe noticeable seasonal fluctuations in vertical time series due to possible recharge. The DInSAR data used in this study and processing files are provided at <http://insar.ca/> to facilitate the MSBAS software use.

## Acknowledgments

We thank the Canadian Space Agency (CSA) for providing RADARSAT-2 data. Figures were plotted with GMT and GnuPlot software and statistical analysis was performed with R software.

## ORCID

Sergey V. Samsonov  <http://orcid.org/0000-0002-6798-4847>

## References

- Beavan, J., Fielding, E., Motagh, M., Samsonov, S., and Donnelly, N. 2011. "Fault location and slip distribution of the 22 February 2011 Mw 6.2 Christchurch, New Zealand, earthquake from geodetic data." *Seismological Research Letters*, Vol. 82(No. 6): pp. 789–799.

- Beavan, R.J., Samsonov, S., Denys, P., Sutherland, R., Palmer, N.G., and Denham, M. 2010. "Oblique slip on the Puysegur subduction interface in the 2009 July Mw 7.8 Dusky Sound earthquake from GPS and InSAR observations: Implications for the tectonics of southwestern New Zealand." *Geophysical Journal International*, Vol. 183(No. 3): pp. 1265–1286. doi: [10.1111/j.1365-246X.2010.04798.x](https://doi.org/10.1111/j.1365-246X.2010.04798.x).
- Berardino, P., Fornaro, G., and Lanari, R. 2002. "A new algorithm for surface deformation monitoring based on small baseline differential SAR interferograms." *IEEE Transactions on Geoscience and Remote Sensing*, Vol. 40(No. 11): pp. 2375–2383.
- Biggs, J., Lu, Z., Fournier, T., and Freymueller, J. 2010. "Magma flux at Okmok Volcano, Alaska from a joint inversion of continuous GPS, campaign GPS and InSAR." *Journal of Geophysical Research*, Vol. 115: pp. B12401. doi: [10.1029/2010JB007577](https://doi.org/10.1029/2010JB007577).
- Bock, Y., Wdowinski, S., Fang, P., Zhang, J., Behr, J., Genrich, J., Williams, S., et al. 1997. "Southern California permanent GPS geodetic array: Continuous measurements of crustal deformation between the 1992 Landers and 1994 Northridge earthquakes." *Journal of Geophysical Research*, Vol. 108: pp. 18,013–18,033.
- Chaussard, E., Wdowinski, S., Cabral-Cano, E., and Amelung, F. 2014. "Land subsidence in central Mexico detected by ALOS InSAR time-series." *Remote Sensing of Environment*, Vol. 140: pp. 94–106. doi: [10.1016/j.rse.2013.08.038](https://doi.org/10.1016/j.rse.2013.08.038).
- Costantini, M. 1998. "A novel phase unwrapping method based on network programming." *IEEE Transactions on Geoscience and Remote Sensing*, Vol. 36(No. 3): pp. 813–821.
- Czarnogorska, M., Samsonov, S., and White, D. 2016. "Airborne and spaceborne remote sensing characterization for Aquistore carbon capture and storage site." *Canadian Journal of Remote Sensing*, Vol. 42(No. 3): pp. 274–290. doi: [10.1080/07038992.2016.1171131](https://doi.org/10.1080/07038992.2016.1171131).
- Ding, X., Chen, Y., Huang, D., Zhu, J., Tsakiri, M., and Stewart, M. 2000. "Slope monitoring using GPS: A multi-antenna approach." *GPS World*, Vol. 11(No. 3): pp. 52–55.
- Dong, S., Samsonov, S., Yin, H., Ye, S., and Cao, Y. 2013. "Time-series analysis of subsidence associated with rapid urbanization in Shanghai, China measured with SBAS InSAR method." *Environmental Earth Sciences*, Vol. 72(No. 3): pp. 677–691. doi: [10.1007/s12665-013-2990-y](https://doi.org/10.1007/s12665-013-2990-y).
- Fournier, T., Pritchard, M.E., and Finnegan, N. 2011. "Accounting for atmospheric delays in InSAR data in a search for long-wavelength deformation in South America." *IEEE Transactions on Geoscience and Remote Sensing*, Vol. 49(No. 10): pp. 3856–3867. doi: [10.1109/TGRS.2011.2139217](https://doi.org/10.1109/TGRS.2011.2139217).
- Gambolati, G., and Teatini, P. 2015. "Geomechanics of subsurface water withdrawal and injection." *Water Resources Research*, Vol. 51(No. 6): pp. 3922–3955. doi: [10.1002/2014WR016841](https://doi.org/10.1002/2014WR016841).
- Goldstein, R., and Werner, C. 1998. "Radar interferogram filtering for geophysical applications." *Geophysical Research Letters*, Vol. 25(No. 21): pp. 4035–4038.
- Gourmelen, N., Amelung, F., Casu, F., Manzo, M., and Lanari, R. 2007. "Mining-related ground deformation in Crescent Valley, Nevada: Implications for sparse GPS networks." *Geophysical Research Letters*, Vol. 34: p. L09309. doi: [10.1029/2007GL029427](https://doi.org/10.1029/2007GL029427).
- Gudmundsson, S., Sigmundsson, F., and Carstensen, J. 2002. "Three-dimensional surface motion maps estimated from combined interferometric synthetic aperture radar and GPS data." *Journal of Geophysical Research*, Vol. 107(No. B10): pp. 2250–2264.
- Hansen, P., and O'Leary, D. 1993. "The use of the L-curve in the regularization of discrete ill-posed problems." *SIAM Journal on Scientific Computing*, Vol. 14(No. 6): pp. 1487–1503.
- Hansen, P.C. 2001. "The truncated SVD as a method for regularization." *BIT*, Vol. 27(No. 4): pp. 534–553. doi: [10.1007/BF01937276](https://doi.org/10.1007/BF01937276).
- Hofmann-Wellenhof, B., Lichtenegger, H., and Collins, J. 2001. *GPS Theory and Practice*. Vienna, Austria: Springer.
- Lanari, R., Mora, O., Manunta, M., Mallorqui, J.J., Berardino, P., and Sansosti, E. 2004. "A small-baseline approach for investigating deformation on full-resolution differential SAR interferograms." *IEEE Transactions on Geoscience and Remote Sensing*, Vol. 42(No. 7): pp. 1377–1386.
- Li, Z., Muller, J.-P., Cross, P., and Fielding, E.J. 2005. "Interferometric synthetic aperture radar (InSAR) atmospheric correction: GPS, moderate resolution imaging spectroradiometer (MODIS), and InSAR integration." *Journal of Geophysical Research*, Vol. 110, p. B03410. doi: [10.1029/2004JB003446](https://doi.org/10.1029/2004JB003446).
- Massonnet, D., and Feigl, K. 1998. "Radar interferometry and its application to changes in the Earth's surface." *Reviews of Geophysics*, Vol. 36(No. 4): pp. 441–500.
- Ortega-Guerrero, A., Cherry, J.A., and Rudolph, D.L. 1993. "Large-scale aquitard consolidation near Mexico City." *Ground Water*, Vol. 31(No. 5): pp. 708–718.
- Ortega-Guerrero, A., Rudolph, D.L., and Cherry, J.A. 1999. "Analysis of long-term land subsidence near Mexico City: Field investigations and predictive modeling." *Water Resources Research*, Vol. 35(No. 11): pp. 3327–3341. doi: [10.1029/1999WR900148](https://doi.org/10.1029/1999WR900148).
- Ortiz-Zamora, D., and Ortega-Guerrero, A. 2010. "Evolution of long-term land subsidence near Mexico City: Review, field investigations, and predictive simulations." *Water Resources Research*, Vol. 46, p. W01513. doi: [10.1029/2008WR007398](https://doi.org/10.1029/2008WR007398).
- Osmanoglu, B., Sunar, F., Wdowinski, S., and Cabral-Cano, E. 2016. "Time series analysis of InSAR data: Methods and trends." *ISPRS Journal of Photogrammetry and Remote Sensing*, Vol. 115: pp. 90–102. doi: [10.1016/j.isprsjprs.2015.10.003](https://doi.org/10.1016/j.isprsjprs.2015.10.003).
- Rosen, P., Hensley, P., Joughin, I., Li, F., Madsen, S., Rodriguez, E., and Goldstein, R. 2000. "Synthetic aperture radar interferometry." *Proc. IEEE*, Vol. 88(No. 3): pp. 333–382.
- Ruiz, G., and Ruiz, R. 2013. "Multi-temporal analysis for Mexico City aquifer." *GeoPlanet: Earth and Planetary Sciences*, Vol. 11: pp. 365–374. doi: [10.1007/978-3-642-30209-1\\_26](https://doi.org/10.1007/978-3-642-30209-1_26).
- Samiee-Esfahany, S., Hanssen, R., van Thienen-Visser, K., and Muntendam-Bos, A. 2009. "On the effect of horizontal deformation on InSAR subsidence estimates." ESA SP-677. Paper presented at the Fringe 2009 Workshop, Frascati, Italy, Nov. 30–Dec. 4, 2009.
- Samsonov, S. 2010. "Topographic correction for ALOS PAL-SAR interferometry." *IEEE Transactions on Geoscience and Remote Sensing*, Vol. 48(No. 7): pp. 3020–3027.
- Samsonov, S., Beavan, J., Gonzalez, P., Tiampo, K., and Fernandez, J. 2011a. "Ground deformation in the Taupo Volcanic Zone, New Zealand observed by ALOS PALSAR interferometry." *Geophysical Journal International*, Vol. 187(No. 1): pp. 147–160.

- Samsonov, S., Czarnogorska, M., and White, D. 2015. "Satellite interferometry for high-precision detection of ground deformation at a carbon dioxide storage site." *International Journal of Greenhouse Gas Control*, Vol. 42: pp. 188–199. doi: [10.1016/j.ijggc.2015.07.034](https://doi.org/10.1016/j.ijggc.2015.07.034).
- Samsonov, S., and d'Oreye, N. 2012. "Multidimensional time series analysis of ground deformation from multiple InSAR data sets applied to Virunga Volcanic Province." *Geophysical Journal International*, Vol. 191(No. 3): pp. 1095–1108. doi: [10.1111/j.1365-246X.2012.05669.x](https://doi.org/10.1111/j.1365-246X.2012.05669.x).
- Samsonov, S., d'Oreye, N., González, P., Tiampo, K., Ertolahti, L., and Clague, J. 2014a. "Rapidly accelerating subsidence in the Greater Vancouver region from two decades of ERS-ENVISAT- RADARSAT-2 DInSAR measurements." *Remote Sensing of Environment*, Vol. 143(No. 5): pp. 180–191. doi: [10.1016/j.rse.2013.12.017](https://doi.org/10.1016/j.rse.2013.12.017).
- Samsonov, S., d'Oreye, N., and Smets, B. 2013a. "Ground deformation associated with post-mining activity at the French-German border revealed by novel InSAR time series method." *International Journal of Applied Earth Observation and Geoinformation*, Vol. 23: pp. 142–154.
- Samsonov, S., Feng, W., Peltier, P., Geirsson, H., d'Oreye, N., and Tiampo, K. 2016a. "Multidimensional small baseline subset (MSBAS) for volcano monitoring in two dimensions: Opportunities and challenges. Case study Piton de la Fournaise volcano." *Journal of Volcanology and Geothermal Research*. doi: [10.1016/j.jvolgeores.2017.04.017](https://doi.org/10.1016/j.jvolgeores.2017.04.017).
- Samsonov, S., Gonzalez, P., Tiampo, K., and d'Oreye, N. 2013b. "Methodology for spatio-temporal analysis of ground deformation occurring near Rice Lake (Saskatchewan) observed by RADARSAT-2 DInSAR during 2008–2011." *Canadian Journal of Remote Sensing*, Vol. 39(No. 1): pp. 27–33.
- Samsonov, S., Gonzalez, P., Tiampo, K., and d'Oreye, N. 2014b. "Modeling of fast ground subsidence observed in southern Saskatchewan (Canada) during 2008–2011." *Natural Hazards and Earth System Sciences*, Vol. 14: pp. 247–257. doi: [10.5194/nhess-14-247-2014](https://doi.org/10.5194/nhess-14-247-2014).
- Samsonov, S., Tiampo, K., and Rundle, J. 2008. "Application of DInSAR-GPS optimization for derivation of three dimensional surface motion of southern California region along the San Andreas fault." *Computers and Geosciences*, Vol. 34(No. 5): pp. 503–514.
- Samsonov, S., Tiampo, K., Rundle, J., and Li, Z. 2007. "Application of DInSAR-GPS optimization for derivation of fine scale surface motion maps of southern California." *IEEE Transactions on Geoscience and Remote Sensing*, Vol. 45(No. 2): pp. 512–521.
- Samsonov, S., van der Kooij, M., and Tiampo, K. 2011b. "A simultaneous inversion for deformation rates and topographic errors of DInSAR data utilizing linear least square inversion technique." *Computers and Geosciences*, Vol. 37(No. 8): pp. 1083–1091.
- Samsonov, S.V., Lantz, T.C., Kokelj, S.V., and Zhang, Y. 2016b. "Growth of a young pingo in the Canadian Arctic observed by RADARSAT-2 interferometric satellite radar." *The Cryosphere*, Vol. 10(No. 2): pp. 799–810. doi: [10.5194/tc-10-799-2016](https://doi.org/10.5194/tc-10-799-2016).
- Samsonov, S.V., Tiampo, K.F., Camacho, A.G., Fernández, J., and González, P.J. 2014c. "Spatiotemporal analysis and interpretation of 1993–2013 ground deformation at Campi Flegrei, Italy, observed by advanced DInSAR." *Geophysical Research Letters*, Vol. 41(No. 17): pp. 6101–6108. doi: [10.1002/2014GL060595](https://doi.org/10.1002/2014GL060595).
- Samsonov, S.V., Tiampo, K.F., and Feng, W. 2016c. "Fast subsidence in downtown of Seattle observed with satellite radar." *Remote Sensing Applications: Society and Environment*, Vol. 4: pp. 179–187. doi: [10.1016/j.rsase.2016.10.001](https://doi.org/10.1016/j.rsase.2016.10.001).
- Samsonov, S.V., Trishchenko, A.P., Tiampo, K., González, P.J., Zhang, Y., and Fernández, J. 2014d. "Removal of systematic seasonal atmospheric signal from interferometric synthetic aperture radar ground deformation time series." *Geophysical Research Letters*, Vol. 41(No. 17): pp. 6123–6130. doi: [10.1002/2014GL061307](https://doi.org/10.1002/2014GL061307).
- Schmidt, D., and Burgmann, R. 2003. "Time-dependent land uplift and subsidence in the Santa Clara valley, California, from a large interferometric synthetic aperture radar data set." *Journal of Geophysical Research*, Vol. 108(No. B9): p. 2416.
- Smets, B., d'Oreye, N., Kervyn, F., Kervyn, M., Albino, F., Arel-lano, S., Bagalwa, M., et al. 2014. "Detailed multidisciplinary monitoring reveals pre-and co-eruptive signals at Nyamulagira volcano (North Kivu, Democratic Republic of Congo)." *Bulletin of Volcanology*, Vol. 76(No. 787): pp. 1–35.
- Strozzi, S., Delaloye, R., Poffet, D., Hansmann, J., and Loew, S. 2011. "Surface subsidence and uplift above a headrace tunnel in metamorphic basement rocks of the Swiss Alps as detected by satellite SAR interferometry." *Remote Sensing of Environment*, Vol. 115(No. 6): pp. 1353–1360.
- Teatini, P., Gambolati, G., Ferronato, M., Settari, A., and Walters, D. 2011. "Land uplift due to subsurface fluid injection." *Journal of Geodynamics*, Vol. 51: pp. 1–16.
- Wegmuller, U., and Werner, C. 1997. "GAMMA SAR processor and interferometry software." Paper presented at the 3rd ERS Symposium on Space at the Service of Our Environment, Florence, Italy, March 17–21, 1997.
- Zhang, J., Bock, Y., Johnson, H., Fang, P., Genrich, J., Williams, S., Wdowinski, S., and Behr, J. 1997. "Southern California permanent GPS geodetic array: Error analysis of daily position estimates and site velocities." *Journal of Geophysical Research*, Vol. 102: pp. 18035–18055.